Radiation pressure and gas drag forces on a melamine-formaldehyde microsphere in a dusty plasma

Bin Liu,[a] J. Goree, and V. Nosenko
Department of Physics and Astronomy, The University of Iowa, Iowa City, Iowa 52242

L. Boufendi
Laboratory GREMI, Université d'Orléans, 45067 Orléans, Cedex O2, France

Measurements are reported for the radiation pressure and gas drag forces acting on a single melamine-formaldehyde microsphere. The radiation pressure force coefficient q, which would be unity if all incident photons were absorbed, has the value $q = 0.94 \pm 0.11$. For argon, the Epstein gas drag force coefficient δ, which would be unity if impinging molecules underwent specular reflection, has the value $\delta = 1.26 \pm 0.13$ as measured with our single-particle laser acceleration method, or $\delta = 1.44 \pm 0.19$ as measured using the vertical resonance method. © *2003 American Institute of Physics.* [DOI: 10.1063/1.1526701]

I. INTRODUCTION

A dusty plasma is an ionized gas containing small particles of solid matter, which are usually charged negatively by collecting electrons and ions from a plasma.[1] Dusty plasmas are of interest in astrophysics and space physics, industrial plasma processing, and laboratory basic plasma physics. Astronomers and space physicists were the first to study this topic because our solar system is full of dusty plasmas such as planetary rings, comet tails, and nebulae. Scientists using industrial plasma processing discovered that particulates suspended in plasma are a major cause of costly wafer contamination during semiconductor manufacturing. Basic plasma physics researchers use dusty plasmas to investigate topics such as waves, instabilities, strongly coupled plasmas, and Coulomb crystallization.

A dust particle can experience numerous forces in a plasma. These include the Coulomb force, gravity, various drag force, and forces driven by optical pressure and temperature gradients. Depending on the type of dusty plasma, however, sometimes only a few of these forces are important. In basic dusty plasma physics experiments, dust particles are often confined by a combination of the Coulomb force and gravity,[2–4] are cooled by gas drag, and can be manipulated by the radiation pressure, ion drag, or thermophoretic forces.

The radiation pressure force is exerted on a particle if it is exposed to a beam of light. For example, the tails of comets always point away from the Sun because of the radiation pressure exerted by sunlight. In laboratory experiments, this force is significant only for very light particles and intense light. This situation arises in colloidal physics, biology experiments,[5,6] and atomic physics.[7] In dusty plasma physics experiments, laser manipulation has been used to induce waves[8–10] and to cause a suspension of particles to rotate.[11] To excite waves, laser manipulation has the advantage, compared with electrical excitation of wave using a metal wire,[12]

that the laser can push dust particles without disturbing the surrounding plasma. Nunomura, Samsonov, and Goree[8] excited the transverse shear wave in a dusty plasma crystal by using a chopped Ar^+ laser beam. Melzer *et al.*[9] and Nosenko and Goree[10] excited Mach cones by using a moving laser beam. Klindworth *et al.*[11] stimulated intershell rotation in a small dusty plasma cluster using a focused laser beam. However, in all these previous experiments, the laser radiation pressure force was not quantified, presumably due to a lack of data. One of our goals in this paper is to measure the force and report the data required for experimenters to quantify their measurements.

The gas drag force is another important force acting on particles. Dusty plasma experimenters have used various formulas for the gas drag[13,14] developed originally by Cunningham,[15] Epstein,[16] Baines,[17] although their original expressions are similar only in limiting cases. For example, in previous experiments with waves[8–10] in dusty plasma, the gas drag force was computed from Epstein's expression but using a coefficient that was not quantified by experiments. Although this coefficient was measured for an oil drop in Millikan's experiment,[18] the coefficient will be different for other substances, depending on how the gas atom interacts with the surface of the particle. For melamine-formaldehyde (MF) microspheres,[19] two experiments have been reported,[20,21] where the coefficient was measured, but their results do not agree. Therefore, a goal of this paper is to report yet another measurement of the gas drag for MF particles.

We chose melamine-formaldehyde (MF) microspheres[19] because they are widely used in dusty plasma experiments. These particles have been used, for example, by groups in Germany to study the crystallization of a dusty plasma and its melting transition,[2,22] in the U.S. to study crystalline structure and waves,[23,24] in Japan to investigate wave in a one-dimensional dust chain,[25] and in the Netherlands to study etching in an oxygen plasma.[26] In analyzing results from all these experiments, authors have been limited in their

---

[a]Electronic mail: bliu@newton.physics.uiowa.edu

calculations of the gas drag force and radiation pressure force because doing so would require precisely measured values of coefficients for melamine-formaldehyde particles, and these have been therefore unavailable. In this paper we report experimentally measured values for these coefficients.

Our goals are to measure the radiation pressure force and the gas drag force acting on a single MF microsphere in a dusty plasma. To do this, we developed a method of computing these forces using the trajectory of a single particle accelerated by a laser beam and its equation of motion. First, we trap a single MF microsphere, which can move easily in horizontal direction but not in vertical direction. Next, the microsphere is accelerated by the radiation pressure force exerted by a laser beam that is turned on and then off. We record the microsphere's trajectory as a time series, and from the time series we will calculate the displacement, velocity and acceleration as functions of time. Finally, we calculate the radiation pressure force, the gas drag force, and also the shape of the confining potential. In some ways, our experiment is similar to a Millikan oil-drop experiment.[27,28] The acceleration and the restoring of the microsphere are similar to the rising and falling of an oil-drop. Like Millikan, we use the equation of motion for a single particle that is subjected to the Coulomb and gas drag forces.

II. FORCES ACTING ON A SINGLE PARTICLE

Here we consider the following forces acting on a single particle in a plasma: Coulomb, gravity, radiation pressure, gas drag, ion drag, and thermophoretic. A particle with a radius r_p, mass density ρ, and charge Q will experience a Coulomb force $Q\vec{E}$ due to an electric field $\vec{E}$, and gravity will be $\frac{4}{3}\pi r_p^3 \rho g$. Note that Q is proportional to the particle's radius r_p, if the radius is much smaller than a Debye length, as it is in our experiments. Thus the Coulomb force will be proportional to the first powers of r_p. Gravity is proportional to the third powers of r_p. For a particle several microns in diameter, gravity is a significant force, while the Coulomb force is important for all particle sizes. Other forces, including the radiation pressure force and gas drag force, which we will measure, are proportional to the second power of r_p. Ion drag is the force exerted on a charged dust particle by flowing ions.[29,30] The thermophoretic force results from a temperature gradient in the neutral gas.

A. Radiation pressure force

Radiation pressure is the momentum per unit area per unit time transferred from photons to a surface. If a beam of photons strikes the particle, some photons will be reflected and others will be transmitted or absorbed. All three processes contribute to the radiation pressure force. In general, for a laser beam of intensity I_{laser}, the radiation pressure force F_{laser} is

$$F_{laser} = q\frac{n_1 \pi r_p^2 I_{laser}}{c}, \tag{1}$$

where n_1 is the refractive index of the medium around the particle and c is the speed of light.

Our first goal in this paper is to measure the coefficient q, which is a dimensionless factor that is determined by the reflection, transmission and absorption of photons on the particle. If all incident photons are absorbed, the value of q will be 1. If they are all reflected, q would be 2 if the particle were a flat disk at normal incidence, and < 2 for any other particle shape. If the microsphere has no significant absorption, only reflection and transmission of light contribute to the radiation pressure force, q will depend on the particle's refractive index n_2. It is noted that q as defined here is different from what is used in the optical tweezers literature, where an efficiency parameter Q depending on the particle size and laser beam profile is used.[31,32] We choose to report q because it is independent of the particle size and laser intensity profile.

B. Gas drag force

The gas drag force is the resistance experienced by a particle moving through a gas. The expression for the gas drag force depends on the particle size and gas atom–atom collision mean free path λ_n. For small particles, $r_p \ll \lambda_n$, moving slowly compared with the gas molecule's thermal velocity, $V \ll \bar{c}$, Epstein's expression[16] is appropriate

$$F_{gas} = \delta\frac{4\pi}{3}Nm\bar{c}r_p^2 V, \tag{2}$$

where, N, m, and $\bar{c}$ are the number density, mass, and mean thermal speed of gas atom, respectively; V is the velocity of the particle with respect to the gas.

Our second goal in this paper is to measure the coefficient δ, which depends on the microscopic mechanism of the collision between the gas atom and the particle surface. In Epstein's model, δ can have a value in the range 1.0–1.442. For specular reflection of all impinging molecules, $\delta = 1.0$. For diffuse reflection with accommodation, $\delta = 1.442$ for a particle made of perfect thermal nonconductor. In general, the exact value of δ must be measured experimentally.

III. SIMPLIFICATION OF EQUATION OF MOTION

Here, we simplify the equation of motion of a single particle by neglecting the forces that are not significant in our experiment. We will begin listing by the forces that we ignore. In Appendix A, we will verify that some of these forces are indeed negligible compared with those we retained in the equation of motion.

In the vertical direction, the particle motion is negligible compared with that in the horizontal direction. We used a radio-frequency plasma, which has a sheath with a very strong vertical electric field that levitates a particle. The particle is trapped in the horizontal direction by a much weaker electric field. The shape of the horizontal electric field is determined in part by a copper ring, which we placed on the top of a lower electrode [see Fig. 1(a)]. Because the sheath conforms to the shape of the electrode surface, the ring helps to shape the sheath like a bowl. This bowl is shallow, so that the single particle can easily move a few millimeters in the horizontal direction. However, the particle was not allowed
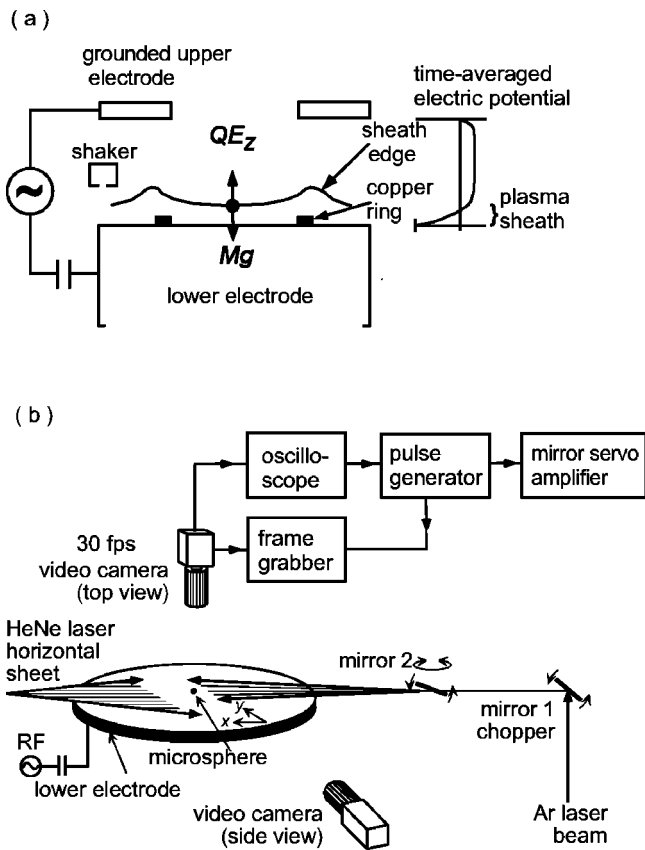
(a)

(b)

FIG. 1. (a) Schematic diagram of a single particle levitated in the sheath in an rf discharge plasma. The sheath edge is shaped by the copper ring on the lower electrode, providing horizontal confinement. (b) Schematic diagram of the experimental setup. A sheet of argon laser light produced by scanning mirror 2 is chopped on and off by scanning mirror 1. A particle is introduced into the plasma by agitating a shaker, and it settles into an equilibrium position above the center of the lower electrode. To allow repeatable trials, the mirror servo amplifier that drives chopper mirror 1 is synchronized to the video camera. The less intense HeNe laser sheet illuminates the particle for viewing with camera.

to move significantly in the vertical direction due to the strong potential well formed by the vertical Coulomb force and gravity.

We neglect any drag forces that are not proportional to the particle's velocity. We expect that the primary drag force will arise from the neutral gas, although we will verify this assumption before computing δ.

The ion drag force is negligible in both the horizontal and vertical directions, although in other experiments it can have substantial effect.[33,34] For our laboratory conditions, with a low ion density, we calculated that in the vertical direction the ion drag force is typically an order of magnitude smaller than gravity. In the horizontal direction, ion drag is similarly less important in our experiment.

The thermophoretic force is neglected in both the horizontal and vertical directions. We assumed that due to the large diameter of our electrode, the gas temperature gradient in the horizontal direction is negligible.

After neglecting these forces, the remaining forces we take into account, for a single particle moving horizontally, are the radiation pressure force, the Coulomb force, and any

drag forces proportional to V. The particle's equation of motion in the horizontal direction is then

$$M\ddot{x}+R\dot{x}-\frac{dU}{dx}=\begin{cases} 0 & \text{laser off} \\ F_{laser} & \text{laser on} \end{cases}, \qquad (3)$$

where x is the particle's position, M is its mass, R is the drag coefficient, U is the potential energy due to horizontal confining potential, and F_{laser} is the laser radiation pressure force.

IV. APPARATUS

We used melamine-formaldehyde (MF) microspheres,[19] with a density of 1.51 g/cm^3. In the experiment, three sizes of particle were used. We measured microspheres' size using transmission electron microscope (TEM), yielding the results in Fig. 2 and Table I.

The experiment was carried out in a GEC reference vacuum cell. Figure 1(b) shows the schematic diagram of our experimental setup. Inside the vacuum cell, there is a lower electrode, which is powered through a capacitor by a radio-frequency (rf) voltage. There is also an upper ring electrode, which serves as the grounded electrode. Between the electrodes, an Ar plasma is formed. On the top of the lower electrode, we placed a copper ring with a thickness of 2 mm and an inner diameter of 65 mm.

We imaged a single microsphere's trajectory using a CCD video camera (top view), with a HeNe laser sheet to illuminate the microsphere. The HeNe laser sheet has a power of 15 mW distributed over a width >100 mm, so its intensity is too small to move the microsphere. The camera operated at 30 frames per second and was equipped with a filter to admit only the He–Ne spectral line. The camera was connected to a frame grabber, and its signal also triggered the mirror servo of Fig. 1(b) to achieve repeatable trials.[9]

The microsphere was manipulated using an Ar$^+$ laser beam. The laser was operated in multiline mode, simultaneously producing several wavelengths in the range of 454.5 nm$<\lambda<$514.5 nm. The intensity profile of the Ar$^+$ laser beam was measured inside the vacuum chamber. Figure 3 shows a typical vertical intensity profile of the laser beam. The circle symbol represents our measurement, and the solid line is a fit to a Gaussian $I_{\text{laser}}\propto\exp(-2z^2/w^2)$, which yields the beam's width w, which is the distance from the center of the beam to the point where the laser intensity is diminished by $1/e^2$. The Ar$^+$ laser beam was expanded into a horizontal laser sheet using scanning mirror 2 of Fig. 1(b).

The laser intensity incident on the microsphere was calculated by modeling the laser sheet's vertical profile as a Gaussian $\propto\exp(-2z^2/w^2)$. We calculated the laser intensity as

$$I_{\text{laser}}=\frac{1.60\,P}{wL}, \qquad (4)$$

where P is the portion of laser's power that is in a uniform region of width L.

We used the vertical resonance method,[21] which was developed originally to measure the particle charge, as an ad-
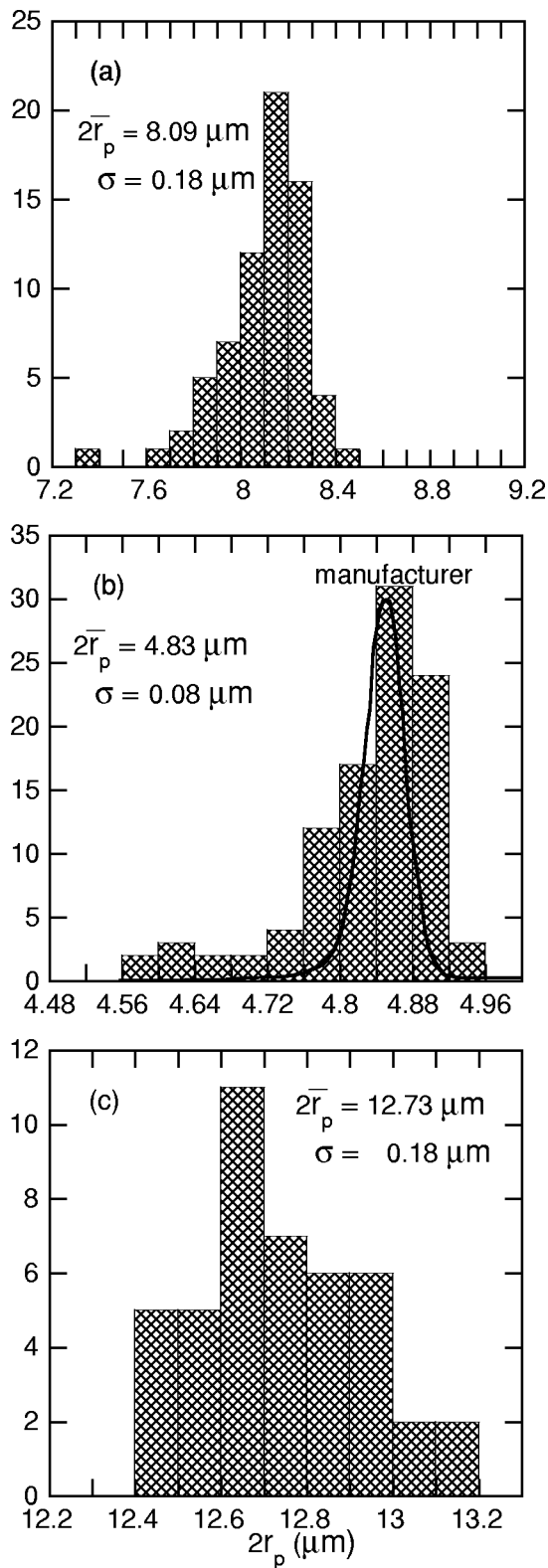
FIG. 2. Size distributions of the melamine-formaldehyde microspheres used in the experiment. The shaded histograms show TEM measurements. For comparison, the curve in (b) is the manufacturer's measurement using a Coulter counter.

TABLE I. Measurement results for MF microsphere's diameter. Values are given for their mean and standard deviation of the mean. We will use our TEM measurements, which differ from the manufacturer's Coulter multisizer measurements.

Method	Particle diameter (μm)		
	#1	#2	#3
Coulter multisizer	5.01 ± 0.08	8.64 ± 0.13	13.8 ± 0.15
TEM (GREMI)	4.83 ± 0.08	8.09 ± 0.18	$12.73 + 0.18$

modulated by a low frequency sine wave, causing the particles to move up and down. Their vertical motion was like a damped harmonic oscillator driven by a time-varying external force. By fitting the amplitude as a function of driving frequency to the form of a damped driven oscillator, this method yields the gas drag coefficient.

V. PROCEDURE

A. Preparing the particle and laser

The first step of the experiment is to introduce a single microsphere into the plasma using a shaker, as shown in Fig. 1(a). The shaker is a cavity with an open side covered by multiple layers of metal mesh, to reduce the number of the microspheres released to the vacuum chamber. To further reduce the number of particles released, the mesh is covered by a metal lid with a hole of diameter ≈ 0.2 mm.

The second step is to align the Ar^+ laser sheet to the height of the microsphere. Because the laser power has a peak in its vertical profile as shown in Fig. 3, we adjust the height of the laser sheet to maximize the brightness of the microsphere.
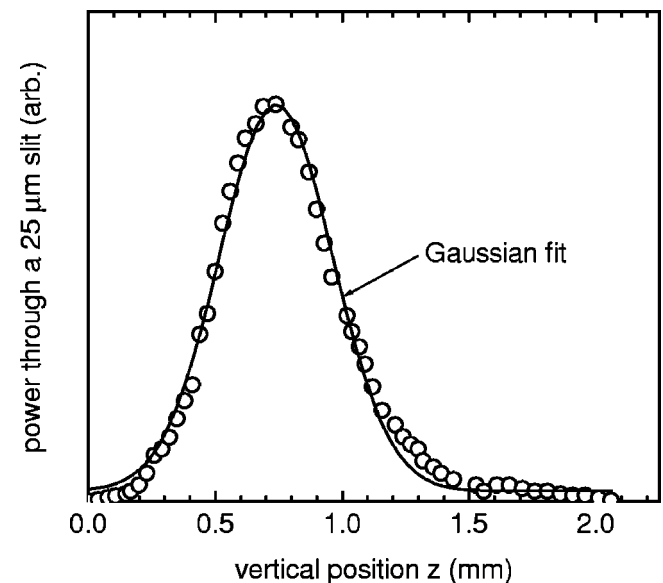

FIG. 3. Vertical intensity profile of the Ar^+ laser beam. The circle represents our measurement using a 25 μm slit, and the solid line is a Gaussian fit yielding the beam's width w. For our laser, w varies slightly with laser power, which was 0.06 Watt for the profile shown here.

ditional method of measuring the gas drag force. In this method, we introduced hundreds of particles to form a monolayer suspension, and we imaged 70 of them with a side view camera. The dc bias of the lower electrode was

B. Imaging and analysis

The images of the microsphere were recorded and digitized using a video camera and a frame grabber. Using a 105 mm focal length Nikon micro lens, the camera has a field of view of 12×9 mm^2. The video signal was digitized by an 8-bit monochrome frame grabber with a rate of 30 frames per second and recorded on the computer as a series of 640×480 pixel images.

The position of the microsphere in each frame was identified by calculating the first moment of the intensity of approximately 25 pixels illuminated by a single particle.[35] This method, which achieves sub-pixel resolution, has the following steps. First, the gray-scale image was converted into a black-and-white image by applying a threshold to identify the contiguous pixels corresponding to a particle. Next, the position (x, y) of the particle was determined as the first moment of pixel intensity, $x = \Sigma_i x_i I_i / \Sigma_i I_i$, where i is the index of a pixel, x_i is the pixel position, and I_i is the pixel intensity. Finally, the positions of the microsphere in different frames were threaded by tracking the images from one frame to next, yielding the microsphere's trajectory x vs t and y vs t.

C. Data processing

We repeated our measurements for different conditions by varying three parameters: Particle size, gas pressure, and laser intensity. We did this for a total of 70 different conditions. For each set of conditions, we repeated the measurement for tens of movies, so that we analyzed a total of almost 500 movies. To reduce the effect of random errors, we averaged the tens of movies for each condition; this was done by averaging the particle position x separately for each frame, $\bar{x}_j = \Sigma_i x_{ij}$, where the subscript i refers to the different movie and j refers to the frame number in a movie. Consecutive frames were used to determine the microsphere's velocity and acceleration using a finite difference method: $\dot{\bar{x}}_j = (\bar{x}_{j+1} - \bar{x}_{j-1})/2\Delta t$ and $\ddot{\bar{x}}_j = (\bar{x}_{j+1} - 2\ddot{\bar{x}}_j + \bar{x}_{j-1})/\Delta t^2$.

D. Calculation of the forces

We developed a scheme to calculate the forces from microsphere's trajectories, using data for the interval when the laser was on and when it was off. The former was 1.0 s, the latter was 3.3 s. First, guessing a value for drag coefficient R, we calculated the potential energy from the microsphere's trajectory during the 3.3 s interval using

$$U(x(t)) = U_0 - \frac{M\dot{x}^2}{2} - R \int_1^t \dot{x}(\tau)^2 d\tau. \tag{5}$$

Second, using the horizontal Coulomb force calculated from Eq. (5) we calculated the radiation pressure force F_{laser} from the microsphere's trajectory during the initial 1.0 s using Eq. (3). Third, we produced a calculated trajectory by solving the equation of motion Eq. (3) during the initial 1.0 s. Finally, we compared the calculated and measured trajectories. We then sought to minimize the squared discrepancy between the trajectories by changing the value of R, and repeating the
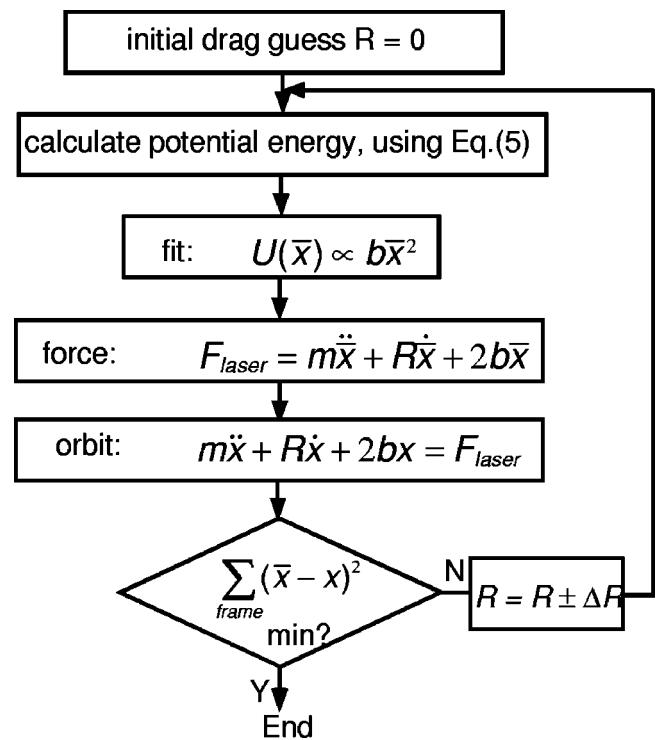

FIG. 4. Flow chart of the calculation of the forces. The data used are time series of the particle's trajectories, averaged over tens of movies for the same condition.

process above until the discrepancy was minimized. The flow chart for this sequence of calculations is shown in Fig. 4.

VI. RESULTS

A. Acceleration of single microsphere by laser radiation pressure force

Generally, the microsphere's motion includes two phases: The acceleration while the laser is on, and the restoration toward the equilibrium position after the laser is off. When the Ar$^+$ laser is on, the microsphere's motion is primarily determined by the radiation pressure force, the drag force, and the horizontal Coulomb force. Initially, the microsphere is accelerated away from its equilibrium position. Once it has moved, it experiences the drag force and the restoring horizontal Coulomb force, which will decelerate the motion. When the laser is off, the microsphere's motion is primarily determined by the drag force and the horizontal Coulomb force. Once it has been restored to its equilibrium position and the motion is damped away, the particle will only undergo random motion, like Brownian motion.

A typical microsphere's displacement in the x direction is shown in Fig. 5 as a function of time. During the initial second, the displacement increases monotonically with time and reaches its maximum value of 2.85 mm; then, after the laser is off, the microsphere returns to its initial position around zero. The maximum displacement is determined mainly by a balance of the laser radiation pressure force and the horizontal Coulomb force.
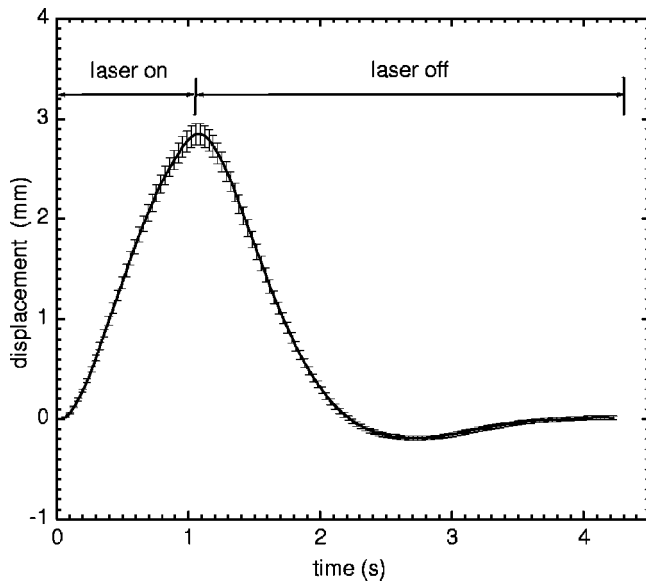
FIG. 5. A particle's displacement as a function of time. We show a line drawn through the data points, with error bars for the standard deviation of the mean.

B. Anomalous trajectories for the largest particle

For our largest particle size, we found two kinds of anomalous trajectories. We recorded trajectories separately for three different particles of nominal diameter 12.57 μm. The first day we used one particle, and for all 35 combinations of gas pressure and laser intensity, the trajectories were mostly as expected, but with some deviation in the y direction, as shown in Fig. 6(a). The second day we used two other particles: Particle (b) in Fig. 6 always exhibited an exaggerated length for its trajectory in the x direction, as well as an irregular motion in the y direction; particle (c) in Fig. 6 always underwent a circular trajectory while the laser was on. We found that these trajectories always had the same kind of anomalous trajectory, for all gas pressure and laser intensity; only the radius of the trajectory varied as we changed these two parameters.

We cannot explain the two kinds of anomalous trajectories exhibited by the largest particle, or why they differ from one particle to another. We can note that particle rotation is observed for non-spherical particle, but our particles, imaged using TEM, appear to be highly spherical.

Hereafter, we will exclude the data from particles (b) and (c). This reduces the usefulness of our data for the largest particle size. However, all our data for the two smaller particle sizes were unaffected.

C. The calculations of the forces

After we have time series for the microsphere's trajectory, we can calculate the forces by following the flow chart described in Fig. 4. In the calculation, the drag coefficient is a fitting parameter which we adjusted to minimize the discrepancy in the particle position.

The calculated laser radiation pressure force is shown in Fig. 7 as a function of time. During the initial second, when the laser is on, our calculated laser radiation pressure force is
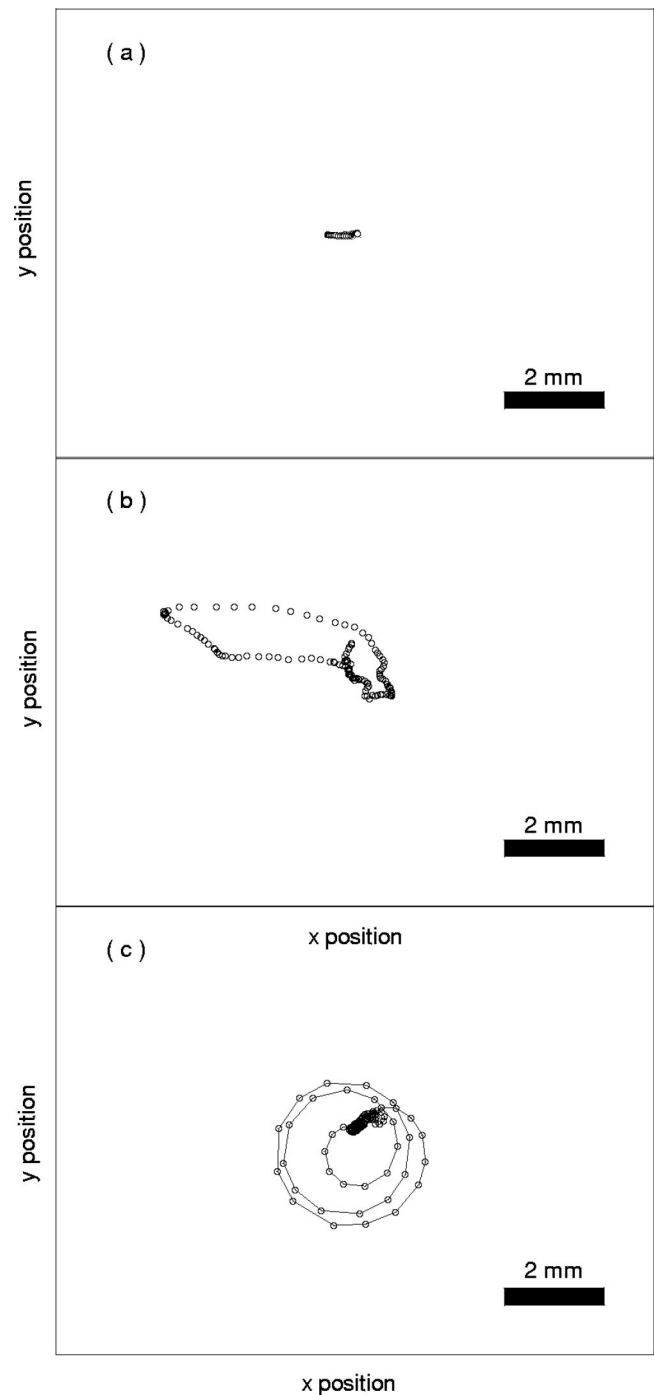

FIG. 6. Representative trajectories for the largest particle size. The trajectory in (a) was as expected, but the trajectories in (b) and (c) were anomalous.

very close to a constant value of about 8.62×10^{-15} N. If our method were perfect the data in the initial second would be exactly a flat line. The noise in the calculated force arises from using the second derivative of the microsphere's trajectories. After the laser is off, the calculated laser force is nearly zero, as shown for $t > 2.5$ s in Fig. 7.

The calculated horizontal potential energy is shown in Fig. 8 as a function of the distance from the microsphere's equilibrium position. This curve is a result of averaging seven potential energy curves, each calculated from data for
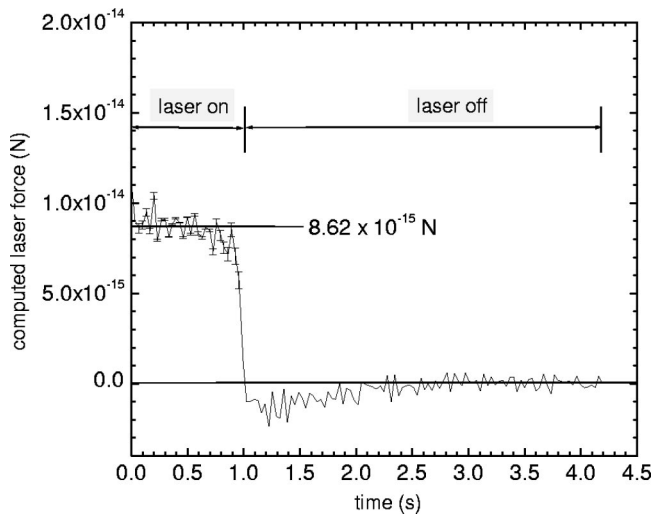
FIG. 7. The calculated laser radiation pressure force as a function of time. Note that the laser radiation force would be constant in the initial second, and zero thereafter, if our method were perfect.

different laser power but the same discharge conditions. It is seen that the confining potential has a parabolic shape. Taking the derivative of the potential energy curve, we can calculate the horizontal Coulomb force, which has a spring constant of about $2.72 \times 10^{-15} \, \mathrm{N \, mm^{-1}}$, for the discharge conditions shown in Fig. 8.

D. Determination of q

Next, we will compute the coefficient q for the radiation pressure force, F_{laser}, and we will also test our results for the expected scaling $F_{\mathrm{laser}} \propto r_p^2 I_{\mathrm{laser}}$. We do this using our results for F_{laser} from Sec. VI C.

Firstly, from the plot of the radiation pressure force vs laser intensity I_{laser}, in Fig. 9(a), we can verify that the only significant external force acting on the particle, other than
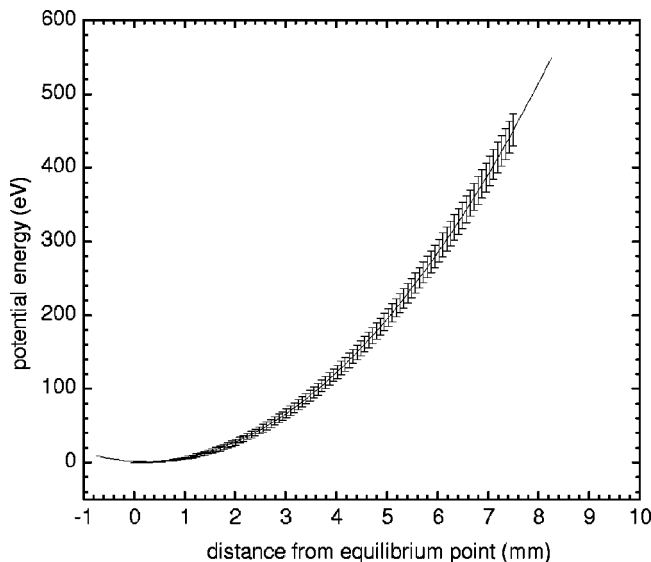
FIG. 8. The calculated horizontal potential energy profile. The equilibrium position is at $x=0$. The data points with error bars represent the measurement, and the solid curve is a fit of the form $U(x) = [8.53(x-0.23)^2 + 0.97] \, \mathrm{eV}$, where x is in mm.
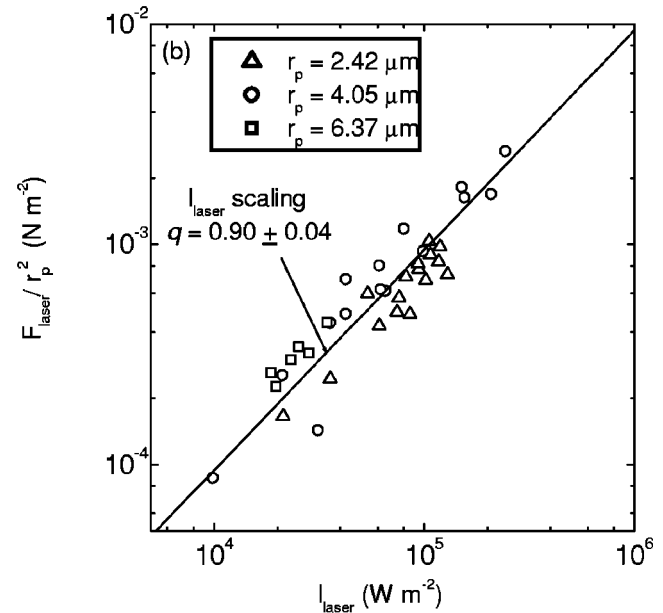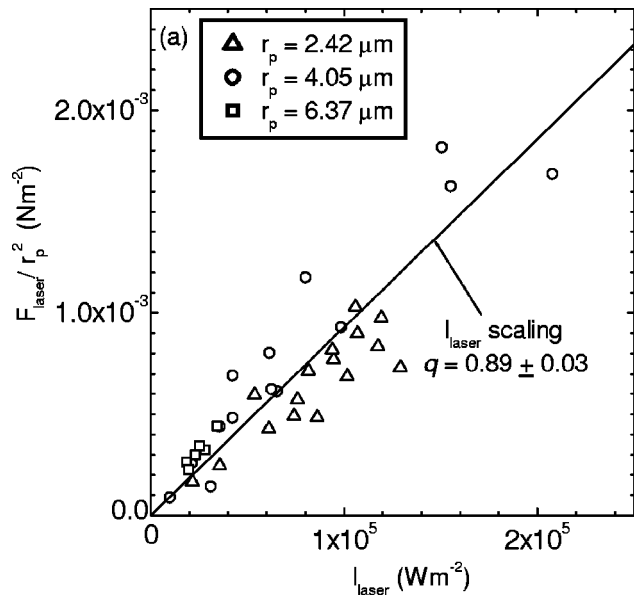
FIG. 9. Laser radiation pressure force as a function of laser intensity. Here, (a) has linear axes, where the fitted line passes through the origin; and (b) has log–log axes, where the fitted line has a slope of unity. Note that the radiation pressure force tends towards zero as the laser intensity is reduced, verifying that the most significant horizontal external force, other than the Coulomb and drag forces, is the radiation pressure force.

the drag force and the confining potential, is the radiation pressure force. We conclude this because the radiation pressure force tends toward zero as the laser intensity is reduced.

We also conclude from Figs. 9(a) and 9(b) that the radiation pressure force is proportional to the first power of the laser intensity, as expected.

We now find values for q, using graphs of the radiation pressure force vs laser intensity, in Fig. 9. We will do this two ways, using the separate graphs with the linear and the log axes. Using the linear axes graph in Fig. 9(a), the data were fitted to a straight line passing through the origin. From the slope of the line we find $q=0.89$. Using the log–log graph in Fig. 9(b), the data were fitted to a straight line with
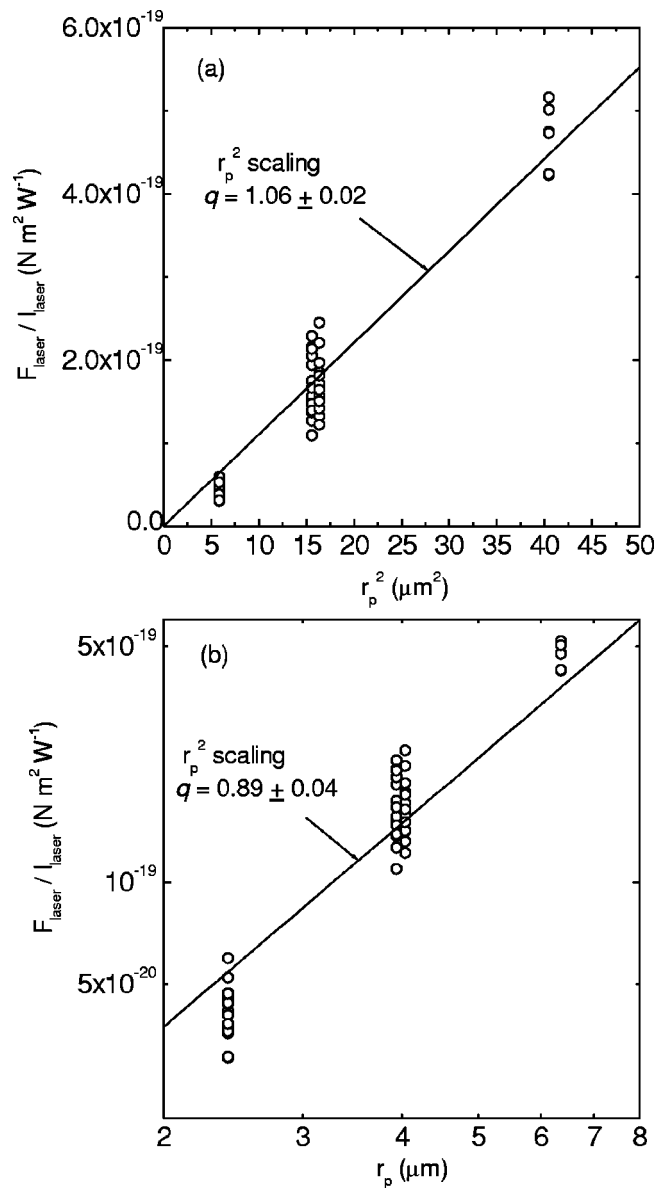
FIG. 10. Laser radiation pressure force as a function of particle size. Here, (a) has linear axes, where the fitted line passes through the origin, and (b) has log–log axes, where the fitted line has a slope of two. The four fits shown here and in Fig. 9 yield four values of the coefficient q, which we average for a final result.

a slope of unity. From the intercept on the vertical axis we find $q = 0.90$.

Secondly, from the plot of the radiation pressure force vs particle size in Fig. 10, we can measure how the radiation pressure force varies with particle size, and obtain two more values for q. Examining Fig. 10(a), we see that the data are fitted reasonably by a straight line. The data shown are limited, however, because we made measurements for only three microsphere's sizes, and the data for the largest of these three sizes is very limited, as explained in Sec. VI B. Only one of the largest particles yielded usable data, providing us a total of six data points in Fig. 10. Because so few data points are presented for the largest particle size in Fig. 10, we suggest that it is not significant that the fit in Fig. 10(b) does not pass through the data points for the largest particle size.

We also conclude from Figs. 10(a) and 10(b) that the radiation pressure force is proportional to the second power of the particle radius, as expected.

We now find the values for q, using graphs of laser radiation pressure force vs particle radius in Fig. 10. We will do this two ways, using the linear and the log axes. For the linear axes graph in Fig. 10(a), the data were fitted to a straight line passing through the origin. From the slope of the line we find $q = 1.06$. For the log–log graph in Fig. 10(b), the data were fitted to a straight line with a slope of two. From the intercept on the vertical axis we find $q = 0.89$.

The reason that our two fitting methods yield different results for q is that in one case we are fitting a straight line on different forms: y vs x and $\log(y)$ vs $\log(x)$. A data point that lies by itself at a large positive value has a smaller effect on the fit result when the fit is performed using log axes, as compared with linear axes. In the case of Fig. 10, the few data points with largest r_p are effectively weighted less heavily in the fit using log axes. Thus, one obtains different results from the two fits, and in general neither result is preferable to the other.

Computing the mean of these four values of q, weighted by their uncertainty, yields our final value $q = 0.94 \pm 0.11$. The calculation of the uncertainty is discussed in Appendix C.

We can compare our experimental result for q with another value predicted using ray optics theory.[31] Our ray optics theoretical calculation, described in Appendix B, yields $q = 0.97$, assuming $n_2 = 1.68$.[26,36] This value is within the range of uncertainty for our measurement.

E. Determination of δ

Here, we will compute the coefficient δ for the gas drag force and test our results for the expected scaling $R \propto p_{gas} r_p^2$. We will do this after we present results that verify that the only damping mechanism is gas drag.

Firstly, from the graph of the drag coefficient R vs gas pressure p_{gas} in Fig. 11(a), we can verify that the only significant damping mechanism is gas drag. We conclude this because the data fall along a straight line passing through the origin. Thus, we can confidently use the Epstein drag model, and proceed to quantify the coefficient δ for Epstein drag.

We also conclude from Figs. 11(a) and 11(b) that the gas drag force is proportional to the first power of the gas pressure, as expected.

We now find the values for δ, using graphs of the drag coefficient vs the gas pressure, in Fig. 11. We will do this two ways, using linear and log axes. For the linear axes graph in Fig. 11(a), the data were fitted to a straight line passing through the origin. From the slope of the line we find $\delta = 1.26$. For the log-log graph in Fig. 11(b), the data were fitted to a straight line with a slope of unity. From the intercept on the vertical axis we find $\delta = 1.15$.

Secondly, from the plot of the drag coefficient vs particle size, Fig. 12, we can measure how the gas drag force varies with particle size, and obtain two more values for δ. Examining Fig. 12(a), we see that the data are fitted reasonably by a straight line, which is consistent with the scaling in Eq. (2).
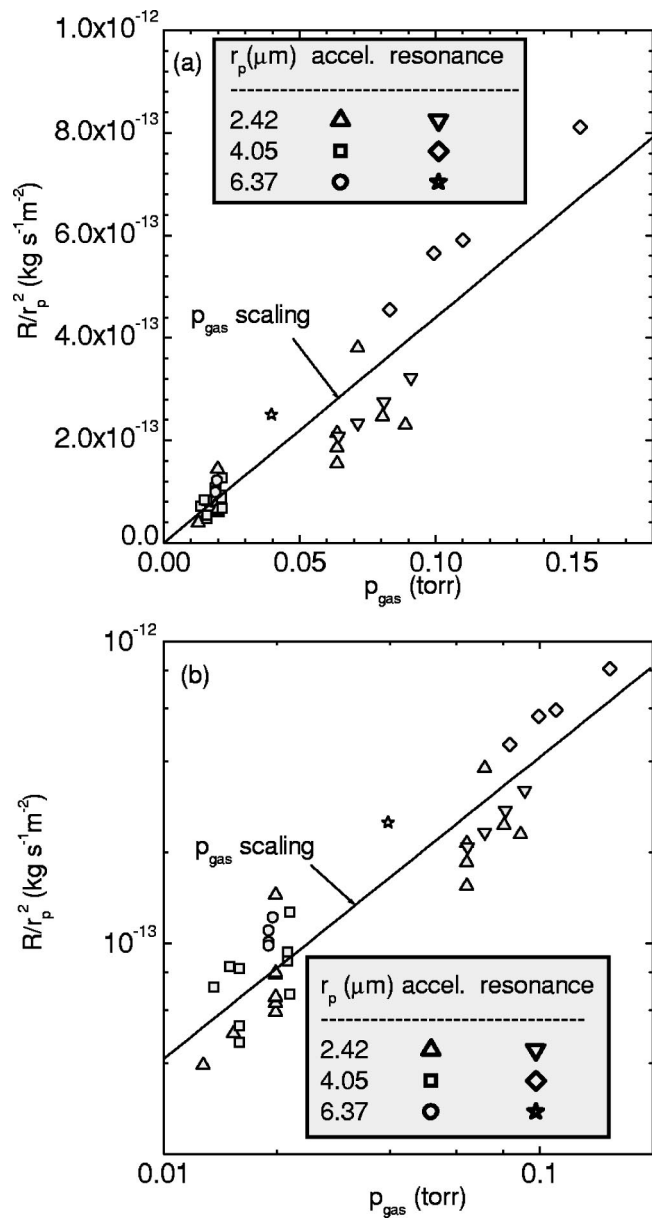
FIG. 11. The drag coefficient R as a function of gas pressure. Here, (a) has linear axes, where the fitted line pass through the origin, and (b) has log–log axes, where the fitted line has a slope of unity. Note that the drag coefficient tends toward zero as gas pressure reduces, verifying that the only drag force that is proportional to the particle velocity is the gas drag force.

FIG. 12. The drag coefficient R as a function of particle size. Here, (a) has linear axes, where the fitted line pass through the origin, and (b) has log–log axes, where the fitted line has a slope of two. The four fits shown here and in Fig. 11 yield four values for the Epstein coefficient δ, which we average for a final result.

However, as mentioned in Sec. VI D, the data for the largest particle size are similarly less reliable, so we suggest that it is not significant that the fit in Fig. 12(b) does not pass through the data points for the largest particle size.

We also conclude from Figs. 12(a) and 12(b) that the gas drag force is proportional to the second power of the particle radius, as expected.

We now find values for δ, using the graphs of the drag coefficient vs particle size in Fig. 12. We will do this two ways, using linear and log axes. For the linear axes graph in Fig. 12(a), the data were fitted to a straight line passing through the origin. From the slope of the line we find $\delta = 1.43$. For the log–log graph in Fig. 12(b), the data were
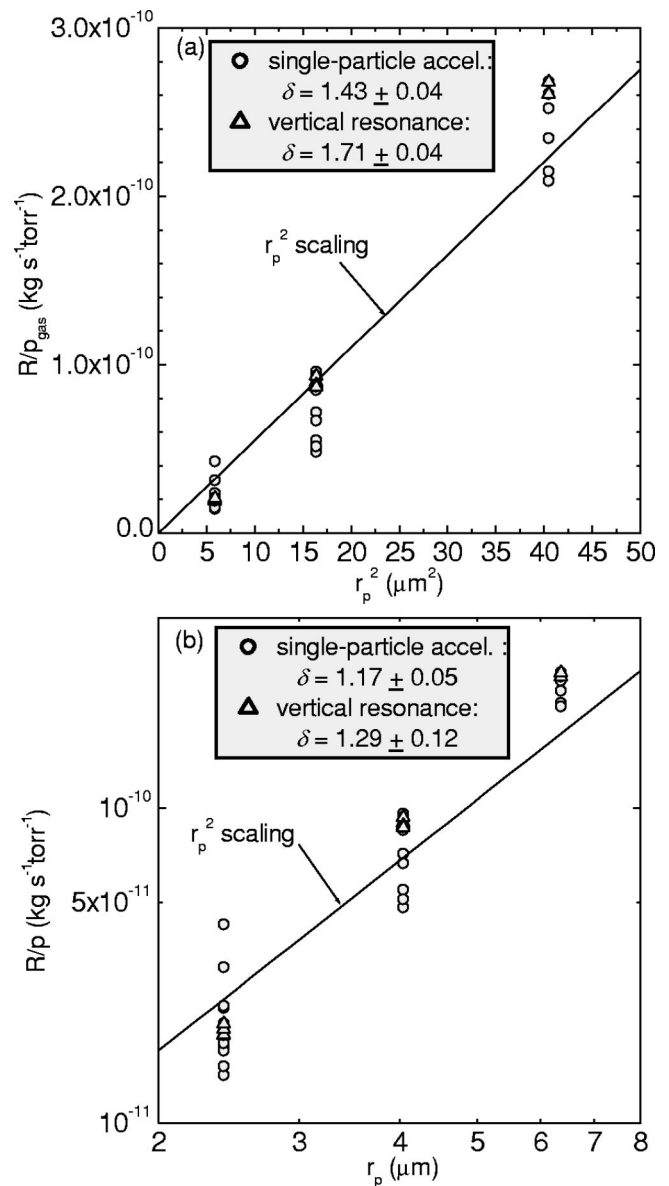
fitted to a straight line with a slope of two. From the intercept on the vertical axis we find $\delta = 1.17$.

Computing the mean of these four values of δ, weighted by their uncertainty, yields our final value, $\delta = 1.26 \pm 0.13$. The uncertainty of this value is discussed in Appendix C.

We can compare this result for δ with a value we measured separately, using the vertical resonance method.[21] This procedure yield the resonance curve in Fig. 13. The experimental data were fitted to a curve $[(\omega_0^2 - \omega^2)^2 + \beta^2 \omega^2]^{-1/2}$, where ω is the modulation frequency, and the fitting parameters are: ω_0, which is the resonance frequency, and β, which is the Epstein drag coefficient. Here we are interested only in β, which yields our drag coefficient $R = M\beta$.

The results of δ from the resonance method are included with our other results plotted in Figs. 11 and 12. Fitting only
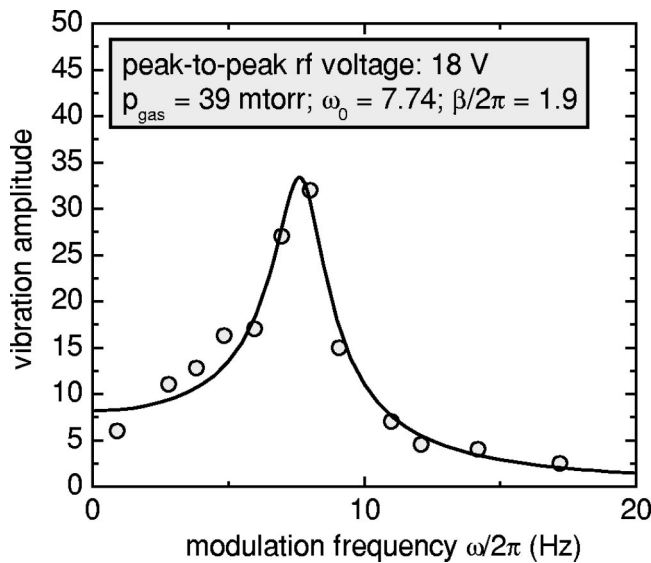
FIG. 13. The amplitude response to the external field as a function of the frequency of the modulation on the lower electrode. Our measurements in this vertical resonance experiment are shown as circles; the curve is a fit of the form $[(\omega_0^2 - \omega^2)^2 + \beta^2 \omega^2]^{-1/2}$. The rf peak-to-peak voltage is 28 V and the Ar gas pressure is 108 mTorr. This fit yields the resonance frequency ω_0 and the Epstein drag coefficient β.

the resonance method data in these graphs, we found four values of δ, which are 1.34, 1.29, 1.71, and 1.29. Computing their mean, weighted by their uncertainty, yields $\delta = 1.44$.

F. Summary of results for q and δ

The final results of our experiment are, for the single–particle acceleration method

$$q = 0.94 \pm 0.11,$$
$$\delta = 1.26 \pm 0.13,$$

and for the vertical resonance method

$$\delta = 1.44 \pm 0.19.$$

The uncertainties listed above were computed in Appendix C.

VII. CONCLUSION

We have reported measurements of the radiation pressure force and the gas drag force acting on a single melamine-formaldehyde microsphere. To do this, we developed a method, single-particle acceleration. Our method assumes that the most important forces acting on the single-particle in the horizontal direction include the Coulomb force, the drag force, and the radiation pressure force due to laser light incident on the particle.

For the radiation pressure force, our measurement verifies that the radiation pressure force is proportional to the incident laser intensity and the particle radius squared. We also generalized our result by measuring a coefficient q.

The value of the coefficient for the radiation pressure force we found is $q = 0.94 \pm 0.11$. We also calculated the coefficient using ray optic theory, and obtained $q = 0.97$, which

is very close to our measurement, assuming that a melamine-formaldehyde microsphere has $n_2 = 1.68$ and no significant absorption.

We verified that the only significant drag force proportional to particle velocity arises from gas. Our measurement verifies that the gas drag force is proportional to the gas pressure and the particle radius squared, as expected from Epstein's theory.

The value of the Epstein coefficient we found is $\delta = 1.26 \pm 0.13$. This result falls within the allowed range of $1 \leq \delta \leq 1.44$ for Epstein's theory. For comparison, we also measured the coefficient using a second method (vertical resonance), yielding $\delta = 1.44 \pm 0.19$.

APPENDIX A: VERIFICATION OF OUR ASSUMPTIONS ABOUT THE FORCES

In Sec. III, we indicated that we would validate these approximations in the Appendix using our results. Here we shall do this, for the representative case of the 8.09 μm particle, which has a mass of 4.18×10^{-13} kg, when it was introduced into a plasma with a 71 V peak-to-peak rf voltage and 13.6 mTorr gas pressure.

Earlier, in Sec. VI, the horizontal Coulomb force was calculated with the assumption that the particle charge is constant during the particle moves. This is because the relative fluctuation of the charge[37] on a dust grain in plasma is small, which was about $\Delta Q / \langle Q \rangle \approx 0.007$ for our case. Moreover, the fluctuation time scale[37] is very short compared with the time scale of the particle motion, so that its effects are averaged away.

Here, we estimate the ion drag in the horizontal direction. We assume: (i) The particle moves along the equipotential plane; (ii) the ion enters the sheath at the ion acoustic speed and it is perpendicular to the equipotential plane; (iii) the radial electric field experienced by an ion is same as that experienced by a particle. The ratio of the horizontal and vertical components of the electric field are estimated by $E_r / E_z \leq 2bx_{max}/Mg$, where the spring constant b of the horizontal Coulomb force was determined in the experiment, and x_{max} is the maximum displacement. The radial velocity of an ion is approximately $v_r \approx c_s E_r / E_z$. Here, c_s is the ion acoustic speed, which is 10^3 m/s if the electron temperature is 1 eV. Thus, the horizontal component of ion drag is $< 3 \times 10^{-16}$ N, which is an order of magnitude smaller than the forces we retained. In calculating the ion drag force, we assumed that the ion density is 5×10^8 cm^{-3}, the ion temperature is 0.05 eV, and the electron temperature is 1 eV.

In the vertical direction, in addition to gravity and the vertical Coulomb force, there will also be ion drag and thermophoretic forces. If the ion has a velocity of about 10^3 m/s, the ion drag will be of the order of 2×10^{-13} N. The thermophoretic force, for $\nabla T = 2.0$ K/cm, [38] will be 3.1×10^{-13} N. These two forces are much smaller than gravity, as shown in Table II.

APPENDIX B: RAY OPTIC CALCULATION

Suppose a uniform and collimated laser beam is incident on a transparent microsphere, as shown in Fig. 14. The laser

TABLE II. Forces acting on a single particle in dusty plasma. The parameters assumed in calculating the results below are: $r_p = 4$ μm, $I_{laser} = 4 \times 10^4$ W m^{-2}, $n_i = 5 \times 10^8$ cm^{-3}, $T_e = 1$ eV, $T_i = 0.05$ eV, $p_{gas} = 14$ mTorr, rf peak-to-peak voltage $= 71$ V.

Horizontal direction	
radiation pressure force	$= 9 \times 10^{-15}$ N
horizontal Coulomb force	$\leq 8 \times 10^{-15}$ N
gas drag force F_{gas}	$\leq 6 \times 10^{-15}$ N
ion drag force	$\leq 3 \times 10^{-16}$ N $\approx 0.05 F_{gas}$
Vertical direction	
gravity $M g$	$= 4 \times 10^{-12}$ N
vertical Coulomb force	$\approx M g$
thermophoretic force	3×10^{-13} N $= 0.08$ Mg
ion drag force	2×10^{-13} N $= 0.05$ Mg

beam will produce two forces: The so-called scattering force, which is parallel to the beam's direction, and the gradient force, which is perpendicular to the beam's direction. Assuming the incident light has a uniform intensity, the gradient force is zero. To calculate the scattering force, we will compute it first for a single ray, and then integrate over all rays incident on the particle. The scattering force F_s due to a single ray of power P is given by[31]

$$F_s = \frac{n_1 P}{c} \left\{ 1 + r \cos 2\theta - \frac{t^2 [\cos(2\theta - 2\gamma) + r \cos 2\theta]}{1 + r^2 + 2r \cos 2\gamma} \right\},$$

where c is light speed in vacuum; θ and γ are the angles of the incidence and the refraction, respectively. The Fresnel coefficients of reflection r and transmission t depend on θ, n_1, and n_2, where $n_1 = 1$ is the refractive index of vacuum and n_2 is the refractive index of the particle. Integrating over θ, to include all rays incident on the particle, the total force is

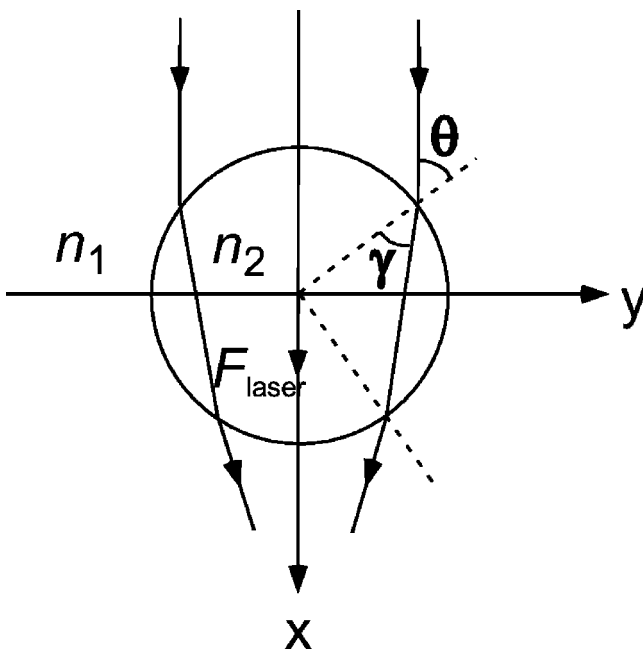FIG. 14. Ray tracing diagram for the refraction of a collimated laser beam incident on a sphere.

$$F_{laser} = \int_0^{\pi/2} F_s I_{laser} 2\pi r_p \sin\theta \, r_p d\theta.$$

APPENDIX C: MEASUREMENT ERRORS

Here we present our method of estimating the measurement errors in our experiments. We include both the systematic errors and the random errors in our final result, using

$$|\Delta u| = \sqrt{(\sigma_u)^2 + (\Delta u)_s^2}. \tag{C1}$$

Here, u represents the variable q or δ. The first term on the right-hand side, $\sigma_u = \sqrt{\Sigma_{i=1}^4 (u_i - \bar{u})^2/4}$, represents the random errors; it is the variance of the measured value of u, and $\bar{u}$ is the weighted mean of the four values obtained from the four fitting methods. The second term, $(\Delta u)_s$, represents the systematic errors of u. We used propagation of error to find the uncertainties.

The largest factor affecting the final error values we report is simply that the data do not fall exactly on a straight line in the Figs. 9–12. Other contributions to the error, which we list below, are rather small.

The uncertainty of the particle size is its standard deviation of mean, determined directly from the distribution of particle sizes as measured by the TEM. The uncertainty of the laser intensity is determined by the uncertainties in the beam's vertical width w, the laser sheet's horizontal width L, the uncertainty of the particle's vertical position in the laser sheet, and the measurement of the power P. The uncertainty in the gas temperature arises from the fluctuation of room temperature, and any heating of the gas due to energetic ion impacting the neutral atoms. According to the simulation of Akdim and Goedheer,[38] ion–neutral collisions give rise to a temperature gradient of at most 2 K/cm in the vertical direction and much less in the horizontal direction. The uncertainty in the gas pressure is due to a small fluctuation of pressure during the course of the experiment despite of using a pressure controller.

We found that the total systematic errors of q and δ are about $|\Delta q/q|_s \approx 0.09$ and $|\Delta \delta/\delta|_s \approx 0.05$, respectively. These systematic errors enter into our final error value, using Eq. (C1), although they contribute less than the corresponding variances arising from the fit.

[1]A. Garscadden, B. N. Ganguly, P. D. Haalard, and J. Williams, Plasma Sources Sci. Technol. **3**, 239 (1994).
[2]H. Thomas, G. E. Morfill, V. Demmel, J. Goree, B. Feuerbacher, and D. Mohlmann, Phys. Rev. Lett. **73**, 652 (1994).
[3]J. Chu and I. Lin, Phys. Rev. Lett. **72**, 4009 (1994).
[4]Y. Hayashi and K. Tachibana, Jpn. J. Appl. Phys., Part 2 **33**, L804 (1994).
[5]A. Ashkin, Proc. Natl. Acad. Sci. U.S.A. **94**, 4853 (1997).
[6]S. M. Block, D. F. Blair, and C. H. Berg, Nature (London) **338**, 514 (1989).
[7]A. H. Anderson, J. R. Ensher, M. R. Mathews, C. E. Wieman, and E. A. Cornell, Science **269**, 198 (1995).
[8]S. Nunomura, D. Samsonov, and J. Goree, Phys. Rev. Lett. **84**, 5141 (2000).
[9]A. Melzer, S. Nunomura, D. Samsonov, Z. W. Ma, and J. Goree, Phys. Rev. E **62**, 4162 (2000).
[10]V. Nosenko, J. Goree, Z. W. Ma, and A. Piel, Phys. Rev. Lett. **88**, 135001 (2002).

[11] M. Klindworth, A. Melzer, A. Piel, and V. A. Schweigert, Phys. Rev. B **61**, 8404 (2000).

[12] J. B. Pieper and J. Goree, Phys. Rev. Lett. **77**, 3137 (1996).

[13] J. F. O'Hanlon, J. Kang, L. K. Russel, and L. Hong, IEEE Trans. Plasma Sci. **22**, 122 (1994).

[14] J. Perrin, P. M. Mata, and P. Belenguer, J. Phys. D **27**, 2499 (1994).

[15] E. Cunningham, Proc. R. Soc. London, Ser. A **83**, 357 (1910).

[16] P. Epstein, Phys. Rev. **23**, 710 (1924).

[17] M. J. Baines, I. P. Williams, and A. S. Asebiomo, Mon. Not. R. Astron. Soc. **130**, 63 (1965).

[18] R. A. Millikan, Phys. Rev. **22**, 711 (1923).

[19] Melamine-formaldehyde microspheres manufactured by micro-particles GmbH, Berlin, Germany, http://www.microparticles.de/.

[20] U. Konopka, private communication, providing data additional to those reported in U. Konopka, G. E. Morfill, and L. Ratke, Phys. Rev. Lett. **84**, 891 (2000).

[21] A. Melzer, private communication, providing data additional to those reported in A. Melzer, T. Trottenberg, and A. Piel, Phys. Lett. A **191**, 301 (1994).

[22] A. Melzer, A. Homann, and A. Piel, Phys. Rev. E **53**, 2757 (1996).

[23] J. B. Pieper, J. Goree, and R. A. Quinn, Phys. Rev. E **54**, 5636 (1996).

[24] D. Samsonov, J. Goree, Z. W. Ma, A. Bhattacharjee, H. M. Thomas, and G. E. Morfill, Phys. Rev. Lett. **83**, 3649 (1999).

[25] T. Misawa, N. Ohno, K. Asano, M. Sawai, S. Takamura, and P. K. Kaw, Phys. Rev. Lett. **86**, 1219 (2001).

[26] W. W. Stoffels, E. Stoffels, G. Swinkels, M. Boufnichel, and G. Kroesen, Phys. Rev. E **59**, 2302 (1999).

[27] R. A. Millikan, Phys. Rev. **11**, 109 (1913).

[28] R. A. Millikan, Phys. Rev. **32**, 349 (1911).

[29] M. Barnes, J. H. Keller, J. C. Forster, J. A. O'Neil, and D. K. Coultas, Phys. Rev. Lett. **68**, 313 (1992).

[30] J. Goree, G. E. Morfill, V. N. Tsytovich, and V. Vladimirv, Phys. Rev. E **59**, 7055 (1999).

[31] A. Ashkin, Biophys. J. **61**, 569 (1992).

[32] A. Ashkin and J. M. Dziedzic, Phys. Rev. Lett. **24**, 156 (1970).

[33] G. E. Morfill, H. M. Thomas, U. Konopka, H. Rothermel, M. Zuzic, A. Ivlev, and J. Goree, Phys. Rev. Lett. **83**, 1598 (1999).

[34] D. Samsonov, A. V. Ivlev, G. E. Morfill, and J. Goree, Phys. Rev. E **63**, 025401 (2001).

[35] D. Samsonov, J. Goree, H. M. Thomas, and G. E. Morfill, Phys. Rev. E **61**, 5557 (2000).

[36] G. H. P. M. Swinkels, E. Stoffels, W. W. Stoffels, N. Simmons, G. M. W. Kroesen, and F. J. De Hoog, Pure Appl. Chem. **70**, 1151 (1998).

[37] C. Cui and J. Goree, IEEE Trans. Plasma Sci. **22**, 151 (1994).

[38] M. R. Akdim and W. J. Goedheer, Phys. Rev. E **65**, 015401(R) (2002).